CHAPTER 4

Temperature Dependent Crystal Structure Transitions and Phase Diagram of (1-x)$Ba(Cu_{1/3}Nb_{2/3})O_3$-(x)$PbTiO_3$ Ceramics

CHAPTER 4.

Temperature Dependent Crystal Structure Transitions and Phase Diagram of (1-x)Ba($Cu_{1/3}Nb_{2/3}$)O_3-(x)$PbTiO_3$ Ceramics

4.1 Introduction

The study of the crystallographic phase stabilities and phase diagram of ferroelectric solid solutions is essential in order to exploit their properties and physical characteristics efficiently. In the phase diagram, the precise location of MPB and the subtle details of the crystal structure near other phase boundaries are of greater significance, since enhanced responses of dielectric and piezoelectric properties may be found in the compositions located near these phase boundaries [85]. The presence of a monoclinic phase at rhombohedral-tetragonal MPB has piqued the interest of researchers over the past a few decades as it is associated with the origin of enhanced responses of piezoelectric and dielectric properties in various solid solutions like PZT and PMN-xPT [86]. In addition to the MPBs and polymorphic phase boundaries (PPBs), the presence of distinct crystallographic phases in compositionally similar materials is also observed in coherent phase interfaces (which have two-phase coexistence of solid solutions in a wide composition ranges than MPBs) [80,87].

As discussed in chapter 1, the solid solution (1-x)BCN-(x)PT have been explored for two compositions only, namely, (0.10)BCN-(0.90)PT and (0.05)BCN-(0.95)PT by Priya et al., for their dielectric, electromechanical and piezoelectric properties [47]. Presence of an anti-ferroelectric phase in the temperature ranges of 400°C-480°C and 450°C-470°C, along with the presence of a low symmetry phase below 60°C and 80°C for (0.10)BCN-(0.90)PT and (0.05)BCN-(0.95)PT, respectively,

have also been predicted by these authors but not confirmed by any diffraction measurements. To the best of our knowledge, no studies on crystal structure, microstructure and ferroelectric properties have been reported in the literature, for complete compositional range of the (1-x)BCN-(x)PT solid solution. In this chapter, the temperature dependent crystallographic phase transitions and structural aspects of various compositions of the (1-x)BCN-(x)PT solid solution have been extensively investigated.

As discussed in the last chapter, the solid solution (1-x)BCN-(x)PT exhibits phase coexistence in the composition range $0.59 \leq x \leq 0.975$ at RT. This chapter is focused on exploring the crystal structure transitions as a function of temperature for many compositions of the solid solution, from cryogenic temperatures (14K) to very high temperatures (1075K). It has been observed that many distinct phase coexistence combinations of the crystal symmetries arise due to crystallographic phase transitions as the crystal structure evolves with temperature. Unambiguous determination of crystal structures has been done by Rietveld Refinement of the XRD patterns recorded by synchrotron XRD and HR-XRD instruments at various temperatures for different compositions.

This chapter is divided into five major divisions. The first Section briefly discusses the temperature-dependent dielectric permittivity behaviour of the solid solution, and the second Section incorporates the temperature-dependent variation in the crystal structures of some selected compositions, where it has been shown that the phase boundaries between them can act like MPBs below the respective pseudocubic transitions. In the third Section, the construction of a phase diagram has been done with the help of XRD, and the gaps have been filled with the approximation through

temperature-dependent dielectric spectroscopy. Finally, in the last Section, the interpretations of the crystal structural behaviour of the solid solution are summarized.

4.2 Temperature-Dependent Analysis of Relative Dielectric Permittivity of (1-x)BCN-(x)PT Ceramics

It is well known for ferroelectric perovskites that, temperature dependence of dielectric permittivity can show anomaly/peak at crystallographic phase transitions due to significant alteration in the unit cell level polarizations. Dielectric permittivity is very helpful in determining the crystal structural transition of phases. It follows a peak appearance near the transition temperature, in both the first and second-order transition in ferroelectric materials. Even though, in some cases, a peak or anomaly can appear in the temperature variation of the permittivity due to dielectric relaxation also. To get an idea about possible temperature dependent structural phase transitions and phase transition temperatures in different compositions of (1-x)BCN-(x)PT ceramics, we performed dielectric measurements on various representative compositions above room temperature. Fig 4.1 shows the temperature-dependent relative dielectric permittivity responses at 10 kHz for these selected compositions. For the composition 0.55, there is no observable peak because it is already in para-electric cubic phase regions at RT. The permittivity response of the 0.55 and 0.65 compositions is very high, mostly due to the high conductivity losses.

Further, it can be seen from Fig 4.1 that, there are two permittivity peaks, for all the compositions, lying between $0.70 \leq x \leq 0.90$ compositions. The low-temperature peaks are marked by red arrows and designated as "T_{M1}", whereas the high-temperature peaks are marked by black arrows and designated as "T_{M2}". As discussed in subsequent sections, the high-temperature XRD studies confirm that these peaks indeed correspond

to the crystal structure transformations of different phases of the solid solution. The composition with x = 0.95 shows only one transition with relatively sharp permittivity peak. In the sections 4.3, the temperature dependent crystal structure evolutions has been shown where the origin of these peaks can be understood well. However, in our case, an unusually complex crystal structure evolution has been encountered with temperature variations. Additionally, the observation of two cubic phases is quite bizarre in comparison to the other similar ferroelectric perovskite materials. To explain the dynamics of the solid solution, the nature of phase transitions in different regions has been explained starting from the 0.90 composition in the following Section.

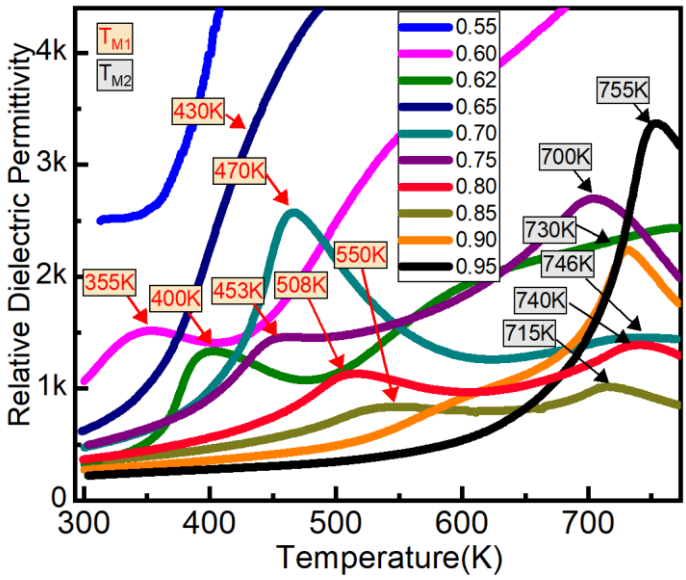

Fig 4.1 Temperature dependence of relative dielectric permittivity of (1-x)BCN-(x)PT ceramic for various compositions (x = 0.55 to 0.95)

4.3 Evolution of Crystal Structure as a function of Composition and Temperature for (1-x)BCN-(x)PT Ceramics

Before discussing the results of temperature dependent phase transitions, the HR-XRD patterns of a few selected representative compositions (x = 0, 0.55, 0.60, 0.62, 0.65, 0.85, 0.90, 1) with distinct crystal structures is reproduced in Fig 4.2(a), for structural evolution at room temperature as a function of composition. The zoomed profiles of (111) and (200) pseudocubic reflection are also shown in Fig 4.2(b and c) to illustrate the development of the RT crystal structure with regard to the composition variation. The distinct phase coexistences have been distinguished from one another by phase boundaries, those are highlighted as horizontal dashed lines in this figure.

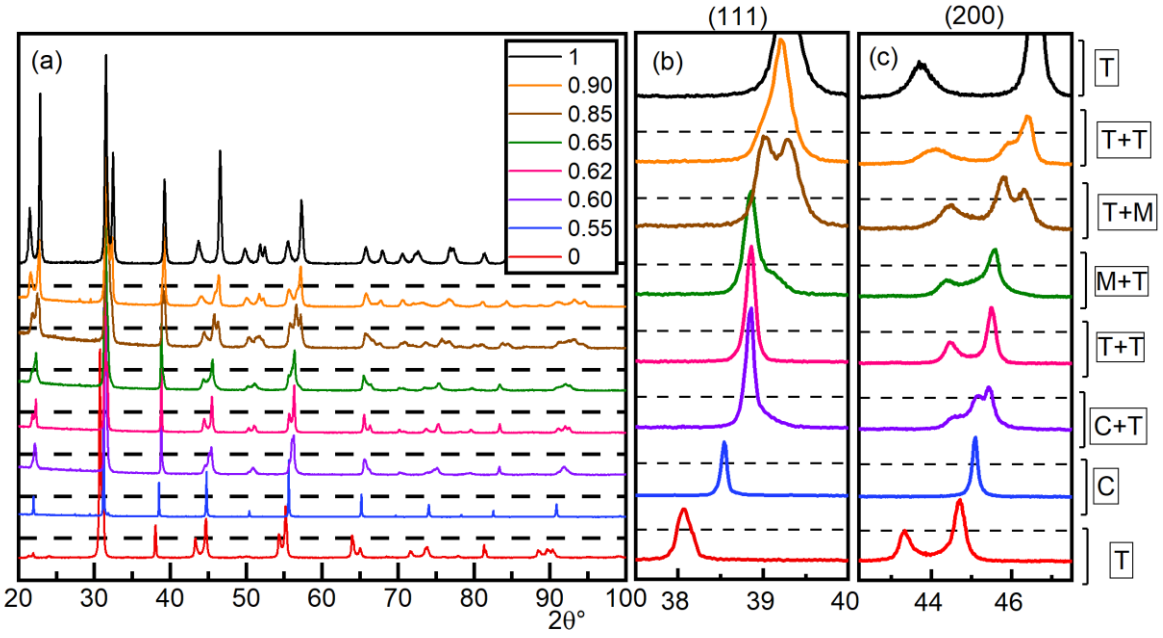

Fig 4.2 Crystal structure evolution with composition at RT. (a) HR XRD patterns of solid solution of (1-x)BCN-(x)PT ceramic for x = 0, 0.55, 0.60, 0.62, 0.65, 0.85, 0.90 and 1. Magnified view of (b) (111) and (c) (200) pseudocubic reflections

Detailed discussion of the RT crystal structure of this solid solution has been already covered chapter 3. In brief, both the end components possess tetragonal symmetry with *P*4*mm* space group. With increasing PT concentration, the solid solution exhibits a cubic structure (*Pm*-3*m)* for $0.05 \leq x \leq 0.55$, a coexistence of cubic and tetragonal structures (*Pm*-3*m* + *P*4*mm*) in the range $0.59 \leq x < 0.62$, coexistence of two tetragonal structures (*P*4*mm* + *P*4*mm*) in the range $0.62 \leq x < 0.65$, a coexistence of monoclinic and tetragonal structures (*Pm*+ *P*4*mm*) in the range $0.65 \leq x \leq 0.85$ and finally the coexistence of two tetragonal structures (*P*4*mm* + *P*4*mm*) in the $0.90 \leq x < 0.975$ composition region. The temperature-dependent phase transitions in of these representative compositions, selected from each of the distinct phases, are studied using Rietveld structure refinements in the subsequent sections. For the temperature-dependent crystal structure evolution study the XRD pattern have been recorded from synchrotron XRD (λ = 1.2286Å) for the compositions x = 0.55, 0.60, 0.62, 0.70 and 0.85, whereas the XRD of the compositions, x = 0.65 and 0.90 have been recorded at a SmartLab 9kW rotating anode Cu-based high-resolution Rigaku diffractometer ($\lambda(K_{\alpha 1})$ = 1.54056Å).

The notations for different profiles and symbols shown in various figures for the Rietveld fit are same as adopted in the last chapter. The symmetry/space group symbols of particular crystal system are mentioned right next to the Bragg's peaks within a framed box while showing Rietveld fit. The quantitative phase fractions of two coexisting phases are also written right next to the corresponding crystal systems adjacent to the Rietveld fit. The temperature of the measurement for XRD data collection is mentioned in the extreme left to a particular pattern while showing the diffraction patterns. The same notations have been used throughout subsections of 4.3 to

illustrate Rietveld fit of different XRD patterns of various compositions at different temperatures. The subscript 1, 2 and 3 have the same annotation as in the last chapter.

4.3.1 Crystal Structures and Phase Transitions in the x = 0.90 Composition

As discussed in chapter 3, the RT crystal structure of the x = 0.90 composition consist of two coexisting phases (T_2 and T_3) both having with *P*4*mm* space group. Fig 4.3(a) shows the Rietveld fits for (111), (200) and (220) pseudocubic reflections of this composition at some selected temperatures from RT to 1073K. The temperature-dependent crystal structure progression reveals interesting phases transitions in this composition. With increasing temperature, the two RT tetragonal structures of this composition persist up to 580K, while the tetragonality reduction takes place at different rates for 'T_2' and 'T_3'. The two phases have almost similar atomic positions in the perovskite structure, having typical $BaTiO_3$-like shifting. In fractional atomic positions of the characteristic perovskite unit cell, the O_1 resides at -0.100(5) for T_2 and -0.122(3) for T_3, while the O_2 resides at 0.587(3) for T_2 and 0.578(3) for T_3. The almost equivalent positions of the anions also reflect the difficulty of identifying the coexisting phases separately at RT. The lattice of T_2 (BCN type) acquires more thermal energy and shows a larger displacement of anions towards the centrosymmetric perovskite positions than 'T_3', and therefore, changes into cubic symmetry at lower temperatures than 'T_3'. Later, near 673K, the tetragonal T_2 transforms into cubic (designated as C_2) and coexists along with the tetragonal (designated as T_3) structure. The second tetragonal phase (T_3) changes to cubic (C_3) structures at 723K, which is not identical to the previously mentioned C_2 phase. Thus, two cubic structures coexist at and above 723K for this composition. The phase coexistence of two cubic phases is visible up to 1073K.

The trends of unit cell volume and phase fraction of the coexisting phases are shown in Fig 4.3(b), while the unit cell parameters are depicted in Fig 4.3(c). The vertical dashed lines represent phase boundaries in these figures, and they are drawn with the help of XRD and dielectric permittivity measurement results. As the temperature rise, due to the increased vibrational energy, obvious phenomenon of ferroelectrics, such as, expansion in the unit cell leading to increased unit cell volume, lowered tetragonality and monotonous increase in lattice parameters are observed as shown in Fig 4.3(b and c). Interestingly, the phase fractions of the two phases do not vary significantly with temperature. The above observation suggests a consideration of phase separation phenomenon in this composition of solid solution. Rietveld Refinement for full diffraction pattern at some selected measurement temperatures, viz., RT, 673K and 1073K, are shown in Fig 4.3(d, e and f).

As investigated by Priya et al. [47], the piezoelectricity for this composition vanishes at 653K. Additional peaks were observed in their studies for ε_r, $\tan\delta$ and k_p near to this temperature, besides the obvious pseudocubic peaks at 700K for PT-like materials. These results are also consistent with our observation of a coexisting cubic structure in the region around the 653K peak, which has led to the vanishing of piezoelectricity. However, it is clear that their anticipation of an antiferroelectric phase between these two transitions (653K – 700K) is merely because of the consideration of the composition as a single thermodynamic entity, instead of two transitions, corresponding to two tetragonal phases, transforming into cubic phases, separately, at two different temperatures. As the presence of phase separation is clear in our HT-XRD measurements, the crystal structure for this temperature region contain two coexisting cubic phases. The region between the two dielectric transitions (~630K and 730K)

reported by Priya et al. [47], is the region corresponding to two transitions of separated phases. Although the observed high-temperature tetragonal (T_3) phase of this temperature region is ferroelectric in nature, yet the absence of ferroelectricity might have arisen due to high losses at such a high temperature.

The refined crystal structural parameters, lattice parameter (a), unit cell volume (V), phase fraction (f) of the coexisting crystal structures for x = 0.90 composition, at different temperatures, are given in Table 4.1.

Table 4.1 The refined crystal structural parameters of various crystallographic phases in x = 0.90 composition (Notations: lattice parameters-a, b, c; unit cell volume-V; phase fraction-f)

Temp. (K)	a_1 (Å)	c_1 (Å)	V_1 (Å^3)	f_1 (%)	a_2 (Å)	c_2 (Å)	V_2 (Å$_3$)	f_2 (%)
300	3.9089(1)	4.1190(2)	62.917(4)	56.52(0.59)	3.9355(2)	4.0786(4)	63.172(7)	43.48(0.71)
473	3.9209(1)	4.0895(1)	62.872(5)	60.32(0.88)	3.9596(2)	4.0417(5)	63.371(11)	39.68(0.88)
573	3.9300(1)	4.0676(2)	62.826(5)	61.50(0.37)	3.9745(3)	4.0172(5)	63.462(11)	38.50(0.36)
673	3.9420(2)	4.0358(2)	62.715(6)	64.51(0.50)	3.9927(2)	3.9927(2)	63.651(6)	35.49(0.20)
723	3.9476(1)	4.0171(3)	62.601(6)	62.24(0.89)	3.9913(2)	-	63.586(6)	37.76(0.36)
773	3.9619(1)	3.9821(1)	62.507(3)	66.59(0.66)	3.9972(1)	-	63.868(5)	33.41(0.24)
873	3.9713(1)	3.9713(1)	62.632(3)	66.20(0.59)	4.0015(1)	-	64.076(5)	33.80(0.23)
973	3.9761(1)	-	62.860(2)	68.10(0.66)	4.0055(1)	-	64.266(5)	31.90(0.22)
1073	3.9818(1)	-	63.131(2)	68.34(0.55)	4.0119(1)	-	64.574(4)	31.66(0.19)

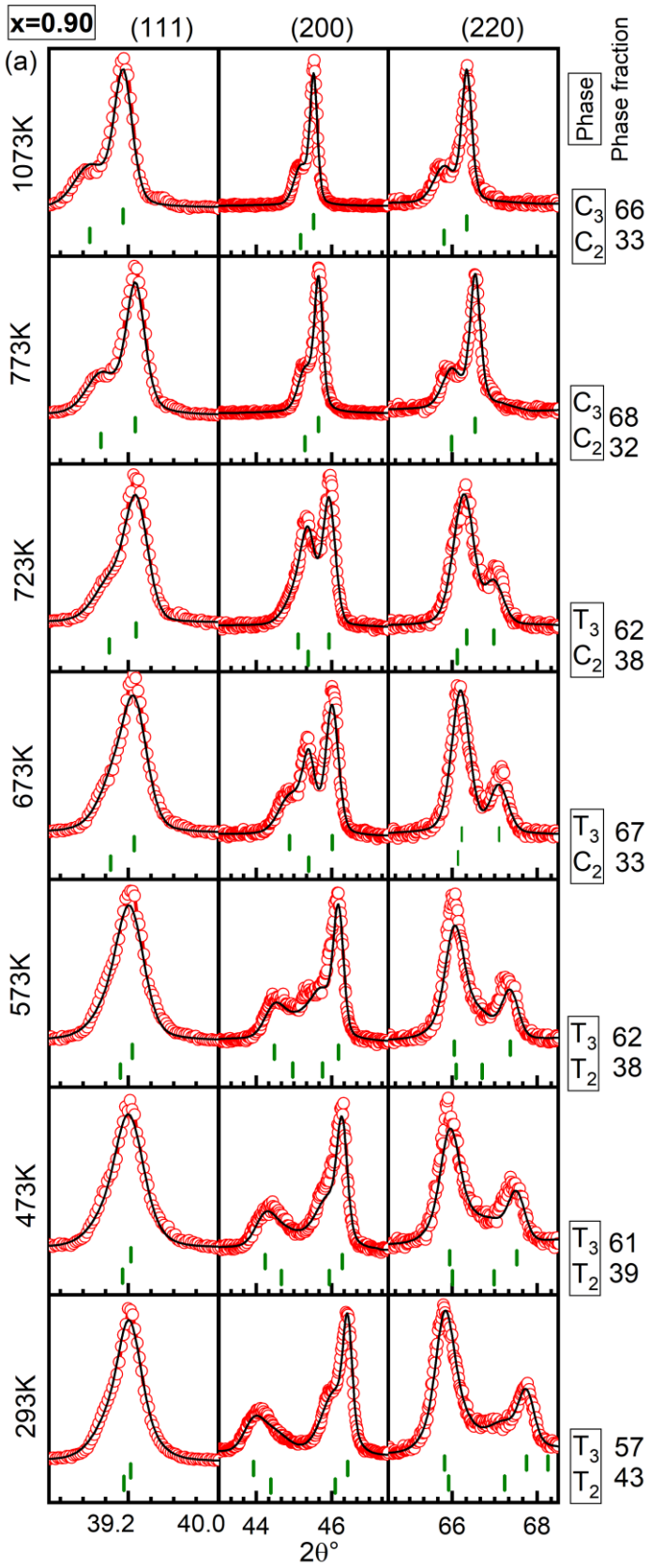

Fig 4.3. (a) Rietveld fits for pseudocubic (111), (200) and (220) XRD profiles at different temperatures for x = 0.90 composition.

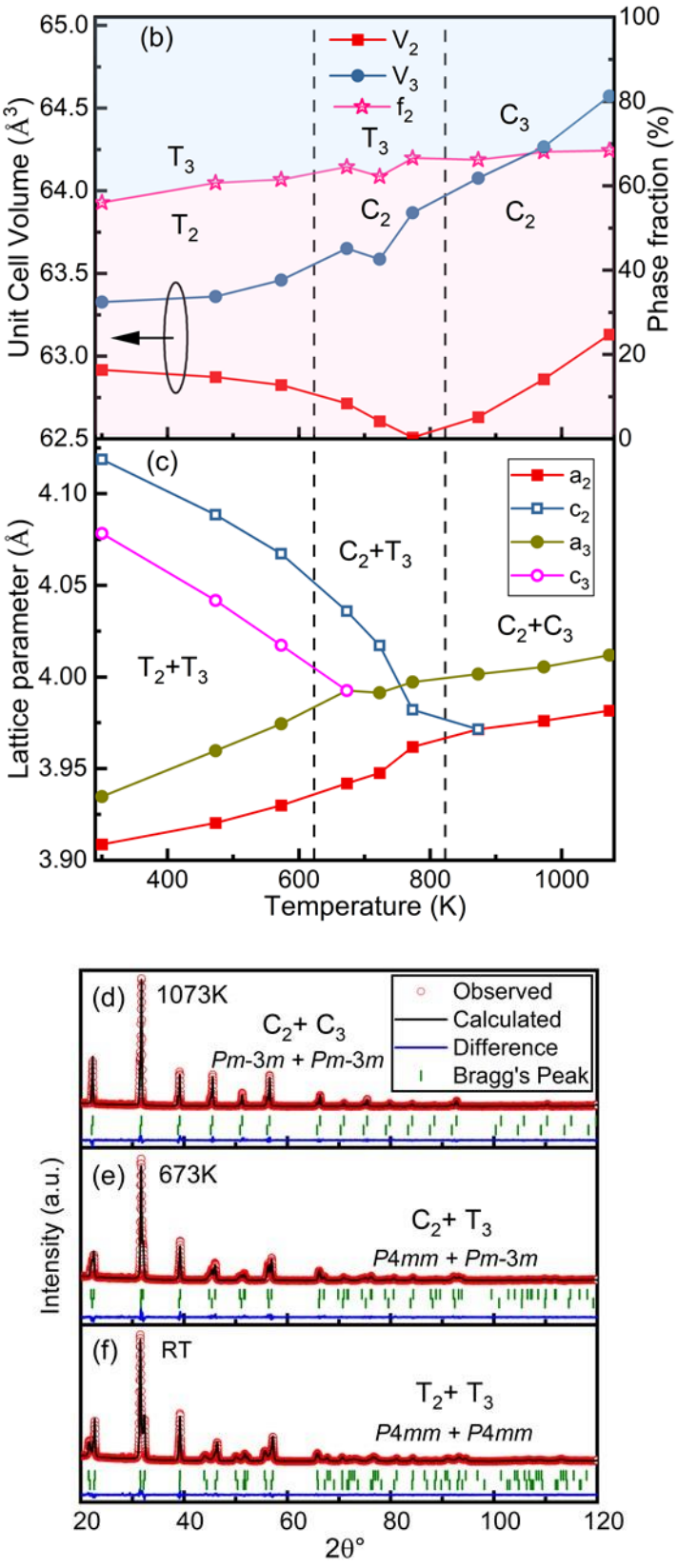

Fig 4.3 Variation of (b) unit cell volume, phase fraction and (c) lattice parameters; Full pattern Rietveld Refinement fits of XRD patterns for (d) 1073K, (e) 673K and (f) RT for x = 0.90 composition.

4.3.2 Crystal Structures and Phase Transitions in the x = 0.85 Composition

Fig 4.4(a) depicts the Rietveld fit and temperature-dependent evolution of the pseudocubic (111), (200) and (220) XRD profiles for the x = 0.85 composition. The crystal structure changes from coexisting tetragonal and monoclinic structures at 15K, to two coexisting cubic structures at 1073K. It is evident from Fig 4.4(a) that the crystal symmetry remains the same in the temperature interval from cryogenic to approximately 550K. The two coexisting structures swiftly accommodate the variation in lattice parameters, especially between 300K and 500K, in which, the 'c' lattice parameter is reduced substantially.

As can be seen from Fig 4.1, the transition temperatures for the x = 0.85 composition are ~550K and ~715K. A careful analysis of the synchrotron XRD data by the Rietveld structure refinement reveals that, the phase transitions of coexisting tetragonal and monoclinic structures also take place separately, after 548K and 723K, respectively. The two cubic phases obtained after successive transformations of the coexisting tetragonal and the monoclinic phases are found to be very stable between 773K and 1073K. Approximately steady phase fraction of the two phases in this temperature range indicates that they do not tend to converge into each other, any sooner, at further higher temperatures. The observation of two cubic phases at such high temperatures is supportive of the unique kind of phase separation phenomenon of this solid solution.

The lattice parameter, unit cell volume and phase fraction variations of the coexisting structures of x = 0.85 composition with varying temperature are illustrated in Fig 4.4(b and c). The corresponding values of these parameters are listed in Table 4.2. Fig 4.4(d) shows the magnified view of (200) pseudocubic reflections of the XRD

pattern at short temperature intervals to show the structure evolution with increasing temperature for x = 0.85 composition. One can observe some small, inconsistent variations in unit cell volume around 200K. Similarly, the phase fractions of the coexisting crystal structures are also observed to be almost constant with a few fluctuations. It may be due to the inaccuracies in the Rietveld Refinement because of highly overlapping XRD peaks are present but no such unusual changes are seen in Fig 4.4(d). Therefore, these fluctuations are not of greater relevance for in-depth inspection.

Depending on how judiciously the measurement temperatures have been selected near the phase transformation temperatures, one can observe three crystallographic structures. An example of such a case is seen for 573K pattern in Fig 4.4(a), where the 'T_2' changes to 'C_2' with the coexistence of these phases along with the 'M_3'. Similarly, the transition of monoclinic structure (M_3) to cubic structure (C_3) must have been mediated through a tetragonal phase, which unfortunately we could not observe due to an inappropriate selection of XRD pattern recording temperature. Measurements at more close temperature intervals will be required to monitor these transitions.

The thermal expansion in the composition is almost negligible in the large temperature range from 15K to approximately 800K. A non-centrosymmetric phase (monoclinic 'M_3") also exists in a much larger temperature range, i.e., from the cryogenic temperatures to ~723K. Both aspects favour the potential of the material in low-fatigue, high-temperature ferroelectric and piezoelectric applications.

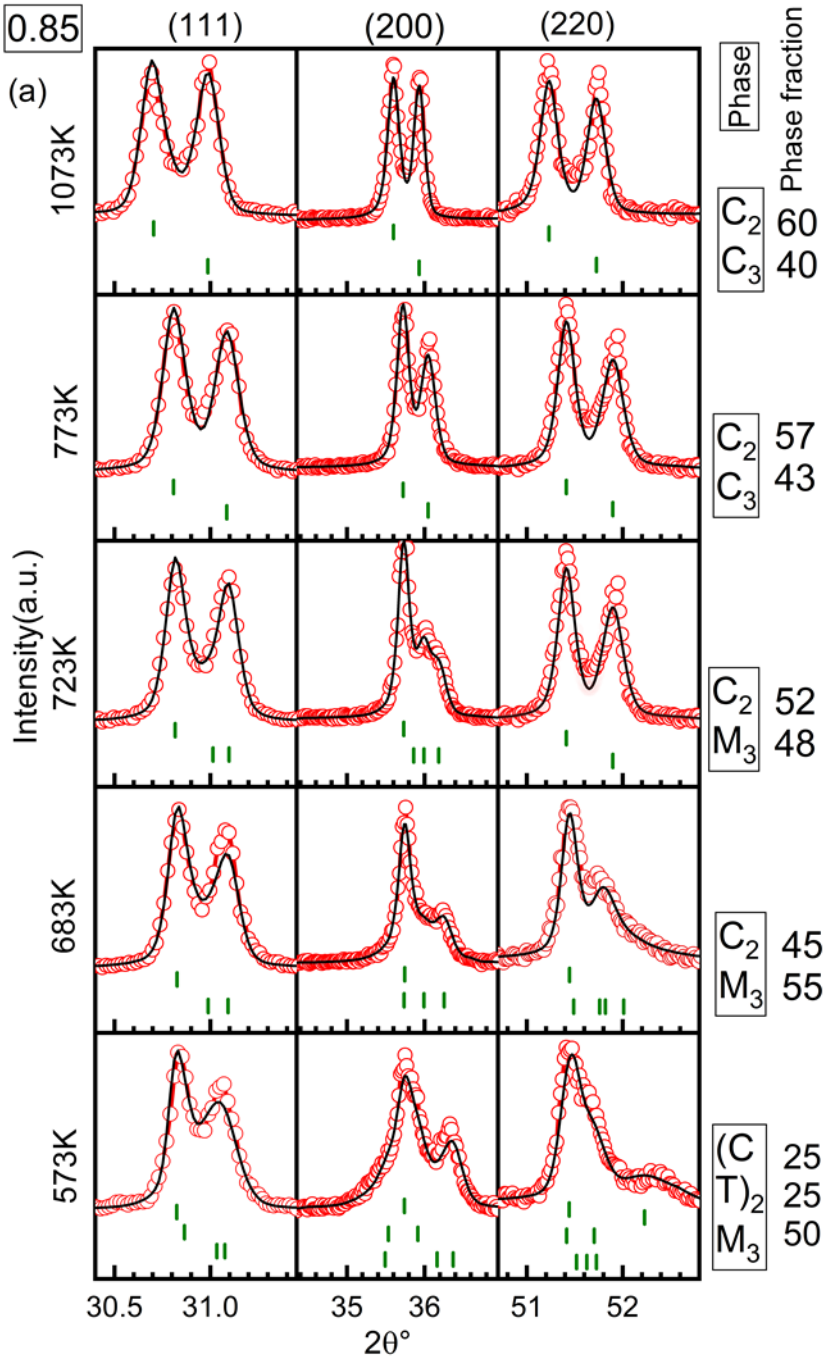

Fig 4.4 (a) Rietveld fit of the pseudocubic (111), (200) and (220) XRD profiles at various temperatures for visualization of the crystal structure evolution with temperature for x = 0.85 composition (Temperature range: 573K-1073K)

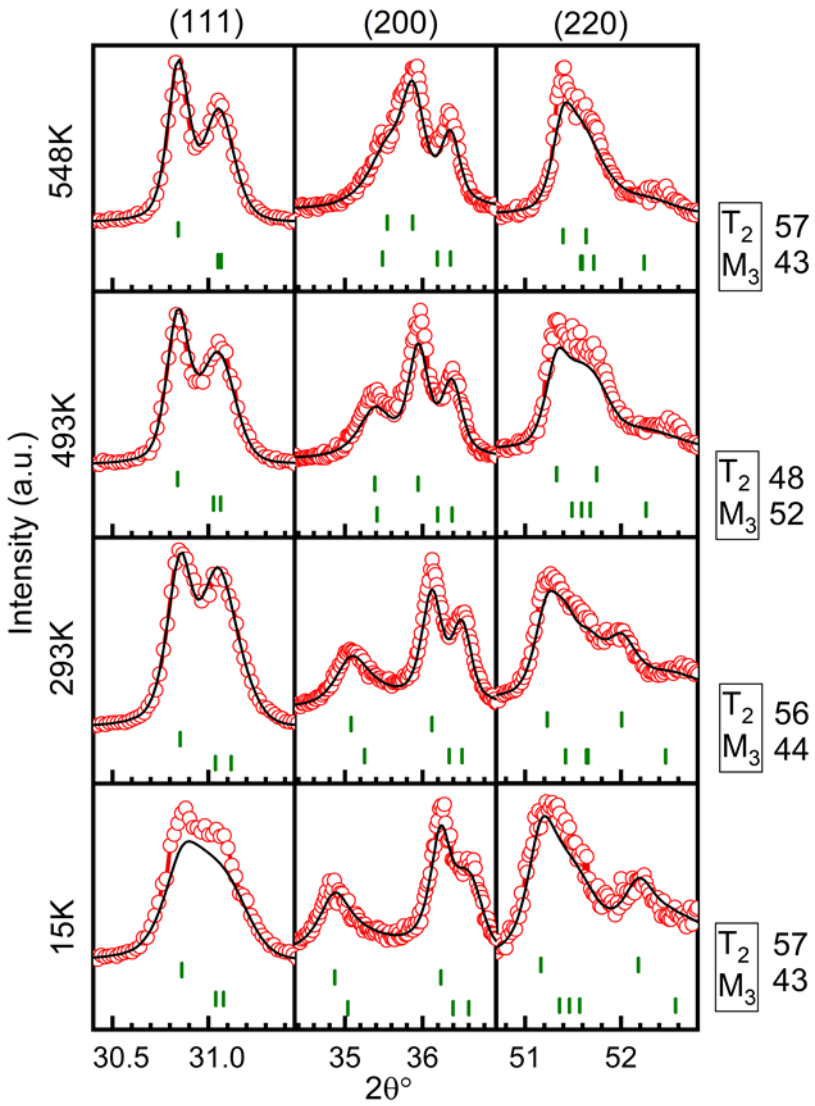

Fig 4.4 (a) Rietveld fit of the pseudocubic (111), (200) and (220) XRD profiles at various temperatures for visualization of the crystal structure evolution with temperature for x = 0.85 composition (Temperature range: 15K-548K)

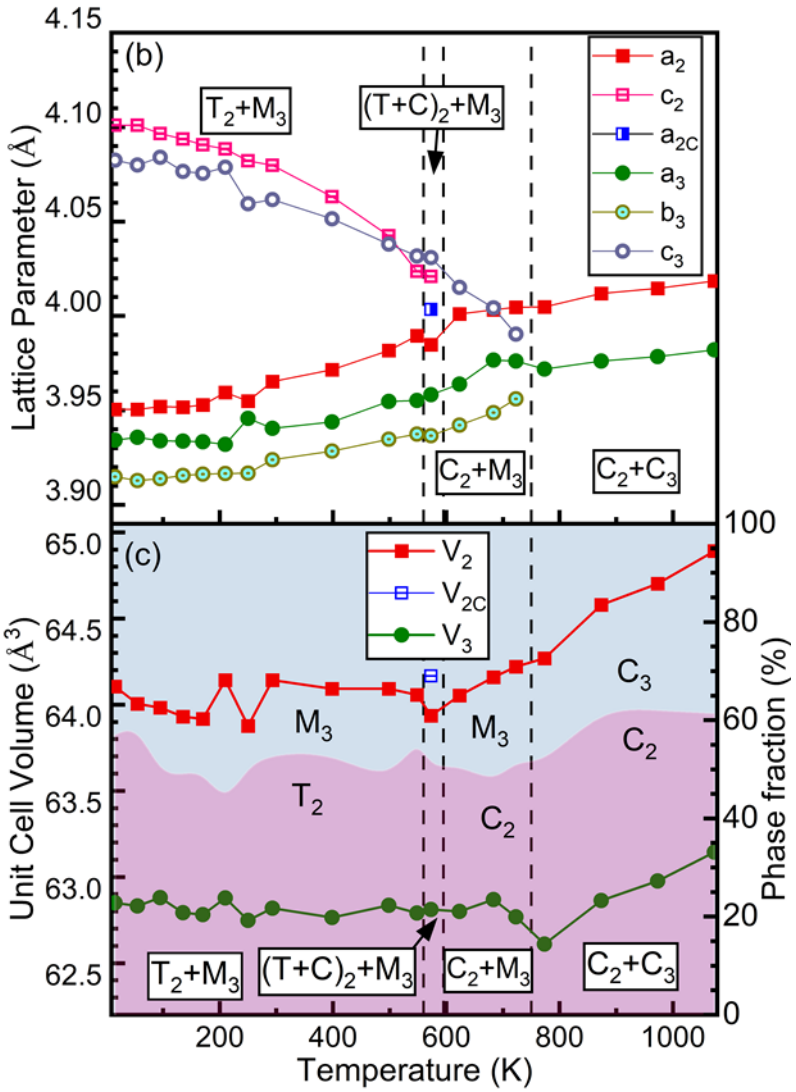

Fig 4.4 Temperature-dependent variation of (b) lattice parameters, (c) unit cell volume and phase fractions for the coexisting phases in x = 0.85 composition

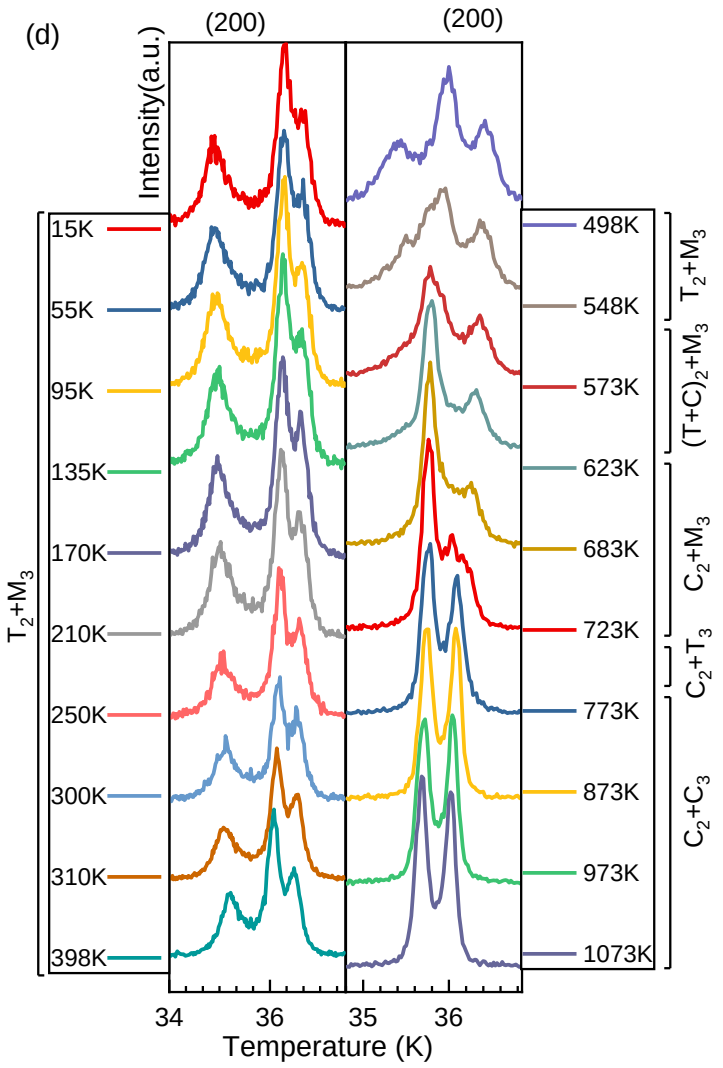

Fig 4.4 (d) Temperature-dependent evolution of the pseudocubic (200) XRD peak at close intervals for x = 0.85 composition

Table 4.2 The refined crystal structural parameters of various crystallographic phases in x = 0.85 composition at different temperatures.

Temp. (K)	a_2/a_{2c} (Å)	c_2 (Å)	V_2/V_{2c} (Å^3)	f_2/f_{2c} (%)	a_3 (Å)	b_3 (Å)	β_3 (°)	c_3 (Å)	V_3 (Å^3)	f_3 (%)
15K	3.9504(3)	4.1009(6)	64.10(1)	57(1.89)	3.9343(9)	3.9148(8)	90.103(8)	4.0824(8)	62.85(2)	43(1.78)
55K	3.950(10)	4.1009(8)	64.00(2)	59(1.45)	3.9358(7)	3.9128(6)	90.103(6)	4.0799(4)	62.83(1)	41(2.03)
95K	3.9520(4)	4.096(7)	63.983(1)	45(1.36)	3.9338(11)	3.9139(6)	89.78(1)	4.0840(9)	62.88(2)	54(1.16)
135K	3.9517(3)	4.0937(5)	63.93(1)	49(1.21)	3.933(10)	3.9156(5)	89.96(1)	4.0765(8)	62.79(2)	51(1.31)
170K	3.9528(4)	4.0906(7)	63.91(1)	49.60(1.82)	3.9334(12)	3.9162(7)	90.05(2)	4.0755(9)	62.78(3)	50.40(2.12)
210K	3.9596(6)	4.0885(7)	64.14(1)	43(2.06)	3.9327(21)	3.9166(5)	90.06(5)	4.0788(9)	62.87(4)	57(1.45)
250K	3.9639(7)	4.0889(10)	63.87(2)	50.67(2.56)	3.9458(11)	3.9210(9)	89.97(7)	4.0735(13)	62.748	48.33(2.67)
RT	3.9652(2)	4.0795(3)	64.14(1)	53.17(0.97)	3.9406(7)	3.9241(4)	90.20(1)	4.0615(5)	62.81(2)	46.83(0.99)
398K	3.9716(2)	4.0632(3)	64.09(1)	53.51(0.45)	3.9439(6)	3.9285(3)	89.86	4.0514(5)	62.76(1)	46.49(0.40)
498K	3.9818(2)	4.0425(4)	64.09(1)	47.08(0.63)	3.9548(8)	3.9347(4)	89.93(4)	4.0379(6)	62.83(2)	52.92(0.63)
548K	3.9895(2)	4.0236(4)	64.05(1)	56.83(2.67)	3.9553(6)	3.9374(3)	90.03(1)	4.0317(6)	62.79(2)	43.17(2.09)
573K	3.98477	4.0266(5)	63.93(2)	24.92(0.84)						
	4.0034(1)	-	64.16(1)	25.34(0.88)	3.9582(5)	3.9367(3)	89.89(3)	4.0308(5)	62.81(2)	49.74(0.73)
623K	4.0011(1)	-	64.05(1)	51.90(0.86)	3.9646(5)	3.9422(3)	89.9341	4.0151(5)	62.81(2)	48.10(0.96)
683K	4.0033(2)	-	64.16(1)	47.13(0.46)	3.9766(5)	3.9488(3)	89.72(1)	4.0043(6)	62.87(2)	52.87(0.51)
723K	4.0046(1)	-	64.22(1)	52.01(0.61)	3.9761(3)	3.9562(2)	89.79(1)	3.9903(5)	62.76(2)	47.99(0.65)
773K	4.0047(1)	-	64.26(1)	60.43(0.76)	3.9718(1)	-	-	-	62.61(1)	39.57(0.60)
873K	4.0120(1)	-	64.57(1)	62.72(0.46)	3.9762(1)	-	-	-	62.86(2)	37.28(0.31)
1073K	4.0185(2)	-	64.89(1)	61.39(0.63)	3.9821(2)	-	-	-	63.14(1)	38.55(0.40)

4.3.3 Crystal Structures and Phase Transitions in the x = 0.65 and 0.70 Compositions

Fig 4.5(a) shows the Rietveld fitted temperature-dependent evolution of pseudocubic (111), (200) and (220) XRD profiles for phase progression in the x = 0.70 composition. Temperature dependent variation of lattice parameters and unit cell volume of different phases for these two compositions, (x = 0.65 and 0.70) are shown in Fig 4.5(b) and Fig 4.5(c), respectively. The RT crystal structure of the 0.70 composition is tetragonal (~93%) and a coexisting minor monoclinic structure (M_3) with ~7% phase fraction. Similar to the x = 0.85 and 0.90 compositions, the x = 0.70 composition also shows negligible changes in the phase fraction of the two coexisting crystal structures as the temperature is varied.

The composition x = 0.70 shows the coexistence of monoclinic (M_3) and tetragonal (T_2) structures from RT to approximately 400K. After 473K, on increasing temperature, the tetragonal (T_{21}) phase fraction eventually decreases, and a simultaneous cubic (C_{22}) structure emerges at the expense of the tetragonal structure (T_{21}). This way, a coexistence of three phases can be seen in the temperature range 400K to 500K. These additional phases (T_{21} and C_{22}) are resulting from the thermodynamic phase transformation of 'T_2' into 'C_2' phase.

Two peaks (470K, 746K) can be seen in Fig 4.1 comprising the dielectric permittivity response for this composition. The former peak (470K) is more prominent and may correspond to the ferroelectric to paraelectric transition for the tetragonal phase due to its higher phase fraction (~94%). The subsequent peak (746K) is broad and might represent a pseudocubic transition related to the monoclinic-tetragonal-cubic crystal structures constituting a lower phase fraction (~6%).

In Fig 4.5(d), the evolution of pseudocubic (111), (200) and (220) reflections of the HR-XRD pattern for the x = 0.65 composition are shown for temperatures ranging from RT to 1073K. The RT crystal structure of a coexisting monoclinic (M_1) and tetragonal (T_2) phases transforms into a coexistence of two tetragonal structures (T_1+T_2) with increasing temperature, and later, around 498K, they merge into a single cubic structure (C_1). Unlike the 0.85 and 0.90 compositions, the phase fractions of the constituent structures do not remain the same as temperature varies. One can notice an additional very low-intensity hump on the higher 2θ angle in the (111) peak from 15K to 1073K. For the crystal structure solution below 698K, this peak is not taken into consideration due to its very low phase fractions. However, its existence is noticeable after 698K as another cubic structure marked by black arrows in Fig 4.5(d). As can be

seen in this figure, its phase fraction is also constant within the shown temperature range and this phase is actually an additional dormant ‘phase-separated’ residuals of PT-like phase observed in dominance for higher PT concentration compositions.

It is noteworthy that the origin of the monoclinic phase in the x = 0.65 composition (M_1) and another monoclinic phase in the x = 0.70 (M_3) composition are quite different, as is the nature of phase coexistence in both the compositions. The phase coexistence in the x = 0.65 composition is the most commonly found first-order thermodynamic phase transition of the ferroelectric perovskites and having both of its coexisting structure originated from BCN-like lattices. In contrast, the phase coexistence of 'T_2' and 'M_3' in the x = 0.70 composition originates from BCN-like and PT-like phases, respectively. This case finds its similarities with quenched and compositionally disordered complex perovskite solid solutions, which can be addressed more appropriately by the term phase separation. As discussed in the previous chapter, this term is also inferred from the unit cell volume difference between the coexisting crystal structures. The composition region $0.80 \leq x \leq 0.90$ of the solid solution possesses significant phase separation from cryogenic to high temperatures in substantial phase fractions of the two coexisting phases, whereas only a small fraction of the phase shows phase separation in the region $0.60 \leq x \leq 0.75$. For the composition region $0.70 \leq x \leq 0.90$, evidently, the phase separation, between the two phases is almost constant with increasing temperature. The refined crystal structural parameters of the x = 0.65 and 0.70 compositions for different structure are listed in Table 4.3 and Table 4.4

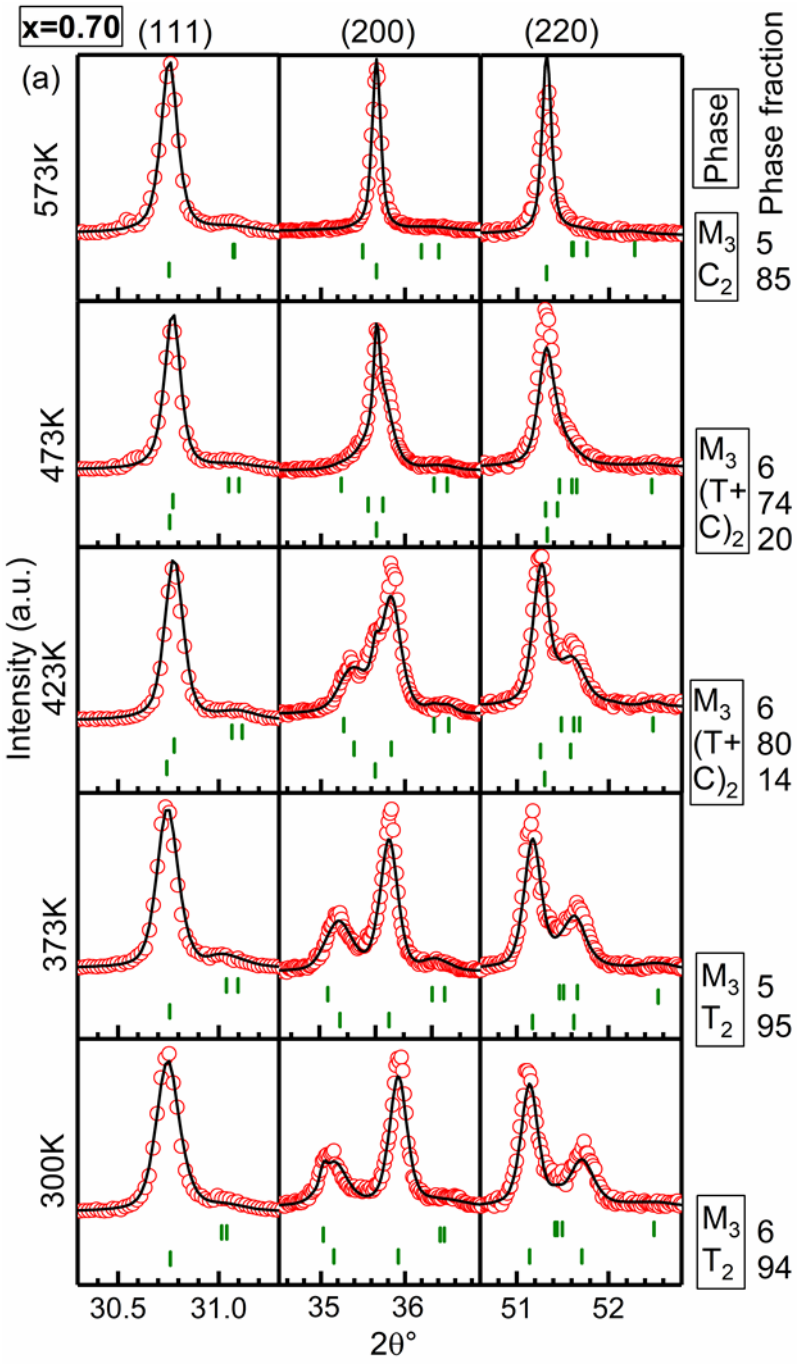

Fig 4.5 (a) Rietveld fit for the pseudocubic (111), (200) and (220) XRD profiles for visualization of the crystal structure evolution with temperature for x = 0.70 composition

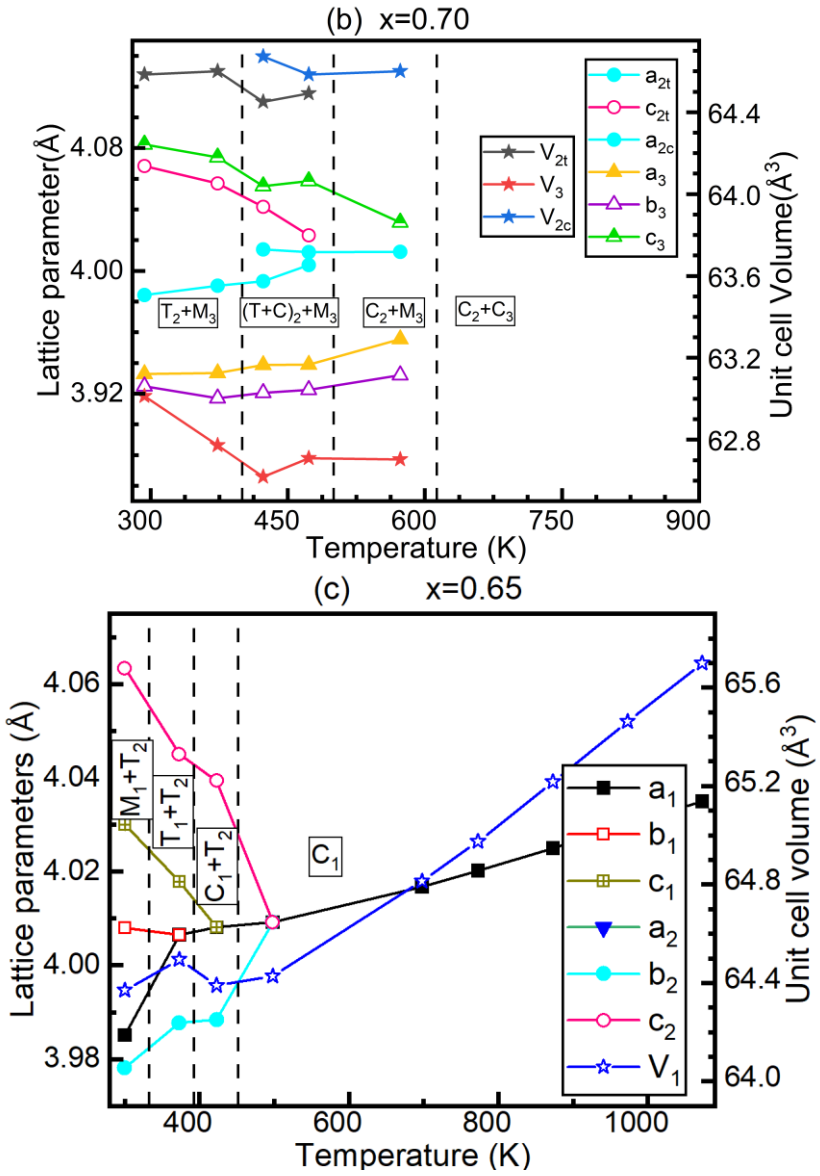

Fig 4.5 Temperature-dependent variation of lattice parameters and unit cell volume for (b) 0.70 composition and (c) 0.65 composition

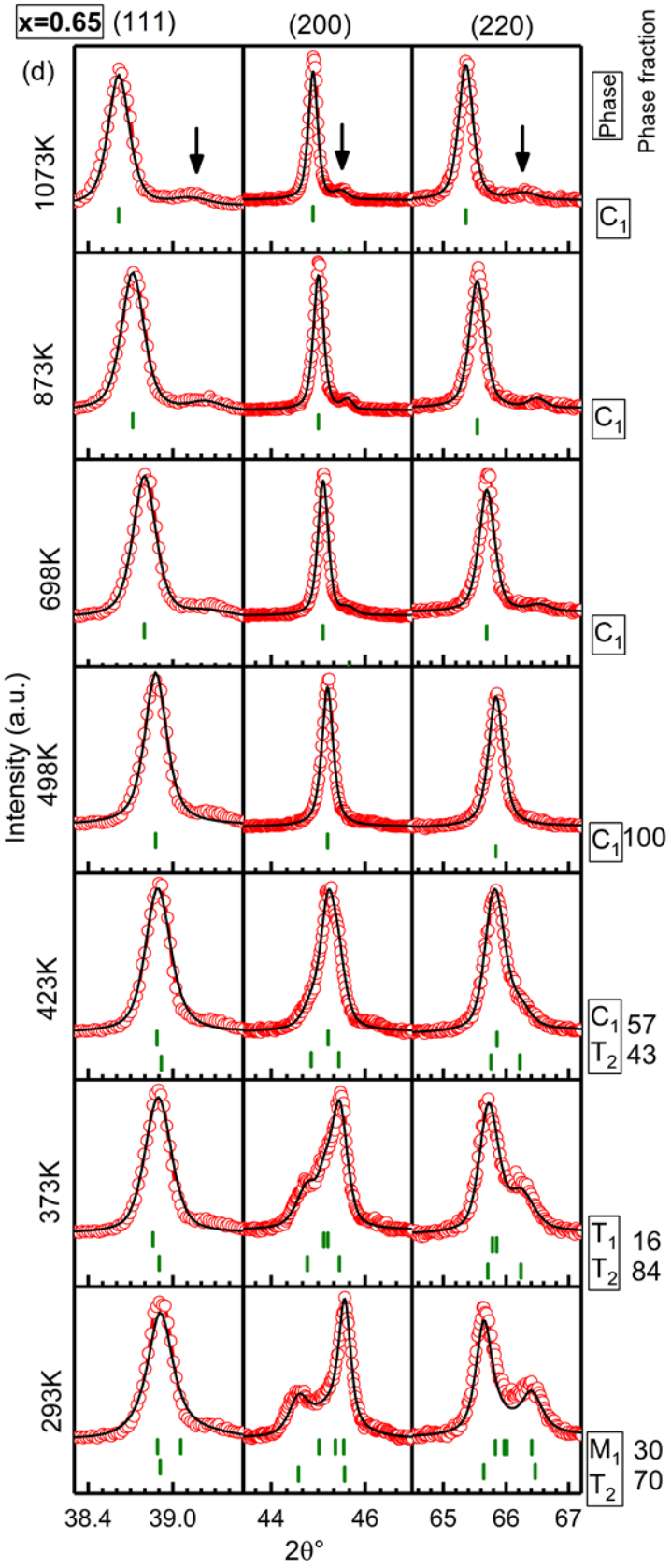

Fig 4.5 (d) Rietveld fit for the pseudocubic (111), (200) and (220) XRD profiles for visualization of the crystal structure evolution with temperature for x = 0.65 composition

Table 4.3 Refined crystal structural parameters of various crystallographic phases in x = 0.70 composition at different temperatures

Temp (K)	a_2 (Å)	c_2 (Å)	V_2 (Å^3)	f_2 (%)	a_3 (Å)	b_3 (Å)	β_3 (°)	c_3 (Å)	V_3 (Å^3)	f_3 (%)	a_{2c} (Å)	V_{2c} (Å^3)
RT	3.9848(1)	4.0688(2)	64.61(1)	92.78(0.85)	3.9278(4)	3.9206(5)	4.0827(2)	90.568(2)	63.45(1)	6.80(0.04)	-	-
373K	3.9904(2)	4.0569(2)	64.60(1)	94.51(0.77)	3.933(1)	3.917(1)	4.074(1)	90.156(2)	62.772	5.49(0.04)	-	-
423K	3.9933(3)	4.0416(4)	64.45(1)	78.95(1.62)	3.938(1)	3.920(1)	4.055(2)	90.135(1)	62.61(3)	7.01(0.12)	4.0139(4)	64.67(1)
473K	4.0038(3)	4.0230(5)	64.49(1)	72.41(1.65)	3.939(2)	3.922(2)	4.058(1)	90.13(5)	62.70(5)	6.32(0.08)	4.0121(2)	64.58(1)
573K	-	-	-	-	3.955(2)	3.932(2)	4.031(2)	89.795(7)	62.70(1)	4.49(0.20)	4.0124(1)	64.65(1)

Table 4.4 Refined crystal structural parameters of various crystallographic phases in x = 0.65 composition at different temperatures

Temp (K)	a_1 (Å)	b_1 (Å)	c_1 (Å)	V_1 (Å^3)	f_1 (%)	a_2 (Å)	c_2 (Å)	V_2 (Å$_3$)	f_2 (%)
RT	3.9850(5)	4.0081(4)	4.03002(4)	64.370(1)	26.66(0.61)	3.9781(1)	4.0633(3)	64.306(6)	73.34(0.84)
373K	4.0065(9)	4.0065(9)	4.0178(21)	64.495(4)	16.09(1.06)	3.9877(1)	4.0450(3)	64.324(6)	83.91(1.39)
423K	4.0081(9)	-	-	64.390(4)	57.03(1.38)	3.9884(3)	4.0393(4)	64.257(10)	42.97(1.20)
498K	4.0089(10)	-	-	64.428(3)	100(0.50)	-	-	-	-
698K	4.0168(1)	-	-	64.813(9)	100	-	-	-	-
773K	4.0202(1)	-	-	64.975(2)	100	-	-	-	-
873K	4.0252(1)	-	-	65.217(2)	100	-	-	-	-
973K	4.0302(1)	-	-	65.462(1)	100	-	-	-	-
1073K	4.0351(1)	-	-	65.700(1)	100	-	-	-	-

4.3.4 Crystal Structures and Phase Transitions in the x= 0.55, 0.60 and 0.62 Compositions

The temperature-dependent crystal structure progressions for the x = 0.62, 0.60 and 0.55 compositions are depicted in Fig 4.6(a), Fig 4.6(b) and Fig 4.6(c), respectively, by showing Rietveld fit of the (111), (200) and (110)/(220) XRD peaks at various temperatures fitted by different plausible crystal structures. As can be seen from Fig 4.6(a), the coexistence of two tetragonal structures is observed from 15K to approximately 293K for the x = 0.62 composition. According to the dielectric permittivity measurement result, the phases transition is this composition takes place around ~400K. Thus, it is reasonable to assume that between 300K and 400K, a

coexistence of cubic and tetragonal phases may be expected. However, in contrast to the structure of compositions discussed earlier, the x = 0.62 composition at higher temperatures transforms into a single cubic phase only.

The crystal structure evolution for the x = 0.60 composition shows the characteristics of two co-existing tetragonal structures from 14K to approximately 200K. The second tetragonal phase with a lower c/a ratio is fitted near the tiny humps of broadened peak tails of the prominent Bragg's peaks of the first tetragonal phase with a higher c/a ratio. The Rietveld analysis of the structure reveals that near to 45K, a monoclinic crystal structure (*Pm*) is slightly more suitable than a tetragonal structure for one of the coexisting tetragonal phases which had lower tetragonality. Thereby, a phase transition sequence of tetragonal-monoclinic-tetragonal phases may take place for phase 1 of this composition with rising temperatures. However, more studies will be needed to precisely ascertain phase transition sequence and phase coexistence in this temperature range. The tetragonal structured phase having a lower tetragonality transforms into a cubic structure near 240K, whereas the other tetragonal phase transforms into cubic symmetry after 358K. A dielectric permittivity peak also appears in Fig 4.1 around 355K for the x = 0.60 composition. For this composition, the cubic phase observed near 240K grows in phase fraction, with increasing temperature and transforms into a single phase near 450K.

The temperature evolution of the pseudocubic (110), (111), and (200) reflections along with the Rietveld fit considering different plausible crystal structures for the 0.55 composition are shown in Fig 4.6(a) in 14K to 300K temperature range. The cubic and tetragonal crystal structures coexist in the temperature range, $14K \leq x \leq 205K$. At further higher temperatures, between $205K < x < 240K$, the tetragonal structure entirely

vanishes, and a cubic structure constitutes the crystal lattice for both at and above RT. Fig 4.6(d), Fig 4.6(e) and Fig 4.6(f) show the temperature-dependent variation of the lattice parameter and unit cell volume obtained from the Rietveld structure Refinement of the x = 0.62, 0.60 and 0.55, compositions, respectively. The corresponding values of these parameters are listed in Table 4.5, Table 4.6 and Table 4.7, for the compositions 0.62, 0.60 and 0.55, respectively. Below RT, the increments in unit cell volume for the x = 0.60 and 0.62 compositions are negligible, while for the x = 0.55 composition, one can see an increase in unit cell volume after 100K. The trends of unit cell volume and lattice parameters, however, do not strictly follow the usual changes resulting from natural thermal expansion. Especially close to the phase transitions, all of these parameters often exhibit a deviation from the monotonous trend due to the lattice instabilities of the phase transitions associated with the development of unit cell polarization.

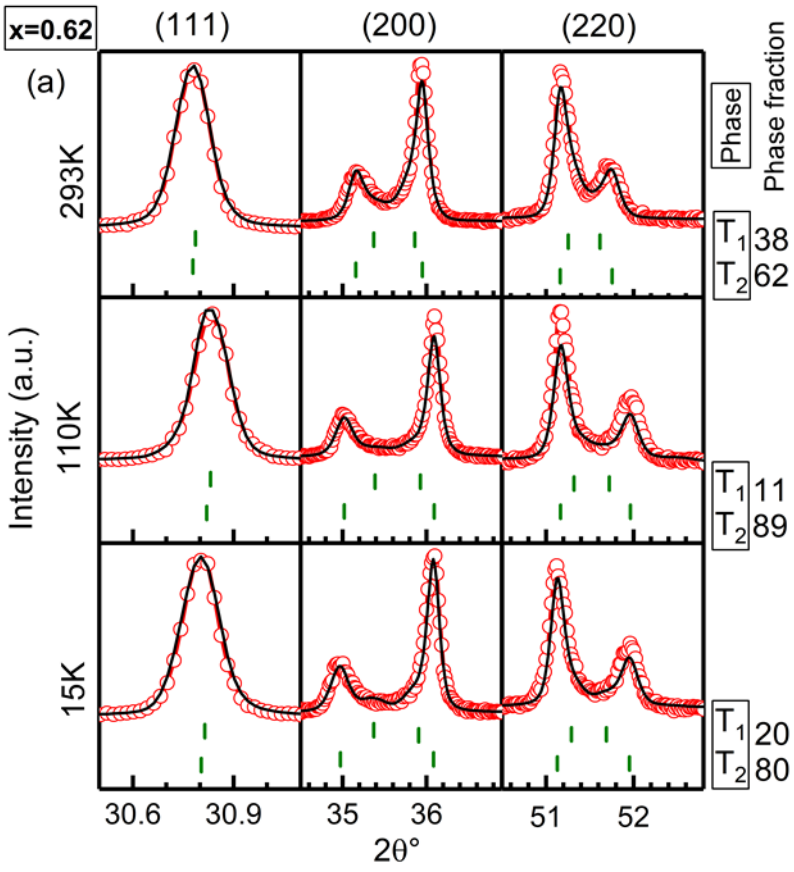

Fig 4.6 (a) Rietveld fit for the pseudocubic (111), (200) and (220) XRD peaks for visualization of crystal structure changes with temperature for x = 0.62 composition

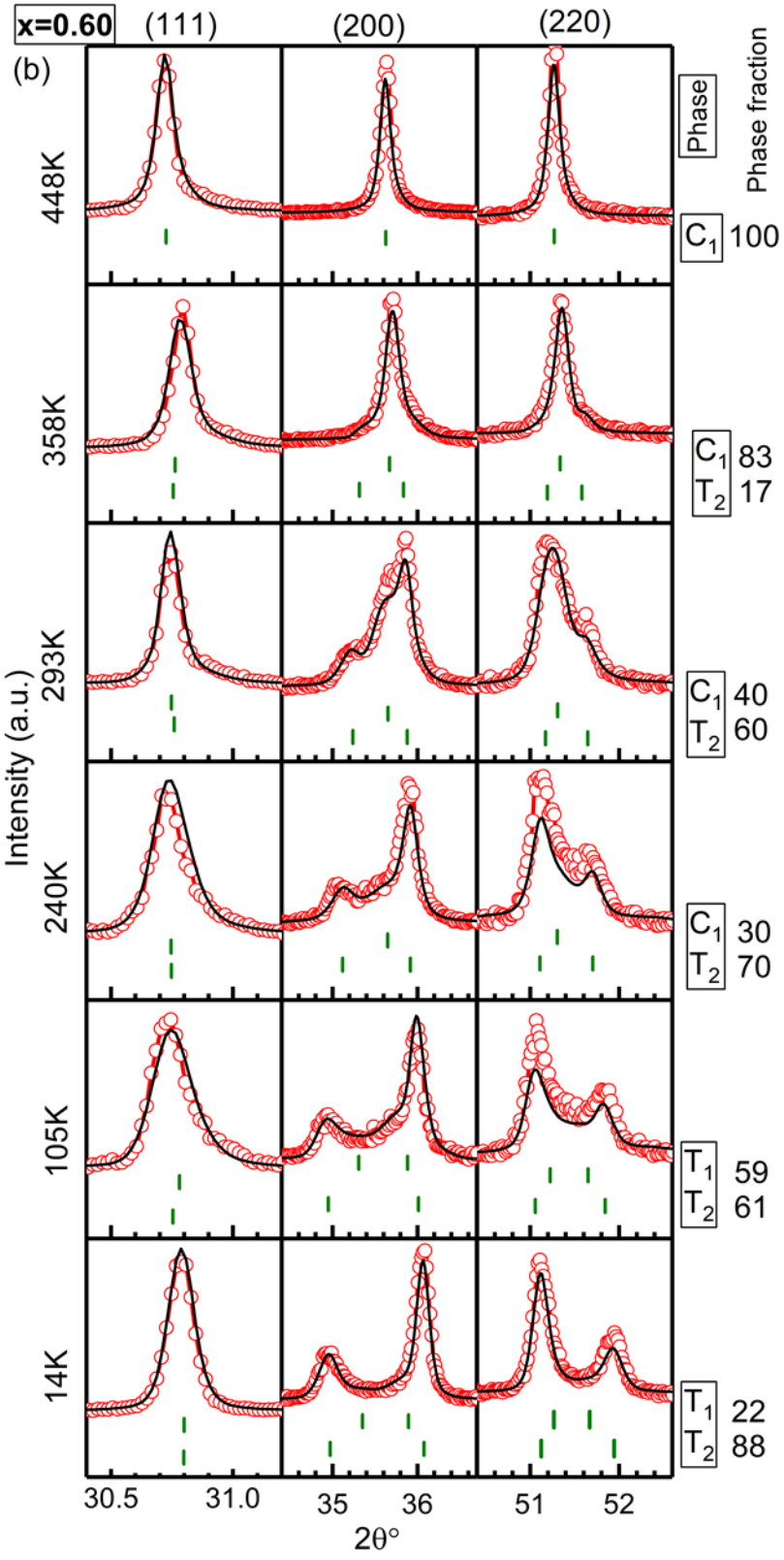

Fig 4.6 (b) Rietveld fit for the pseudocubic (111), (200) and (220) XRD peaks for visualization of crystal structure changes with temperature for x = 0.60 composition

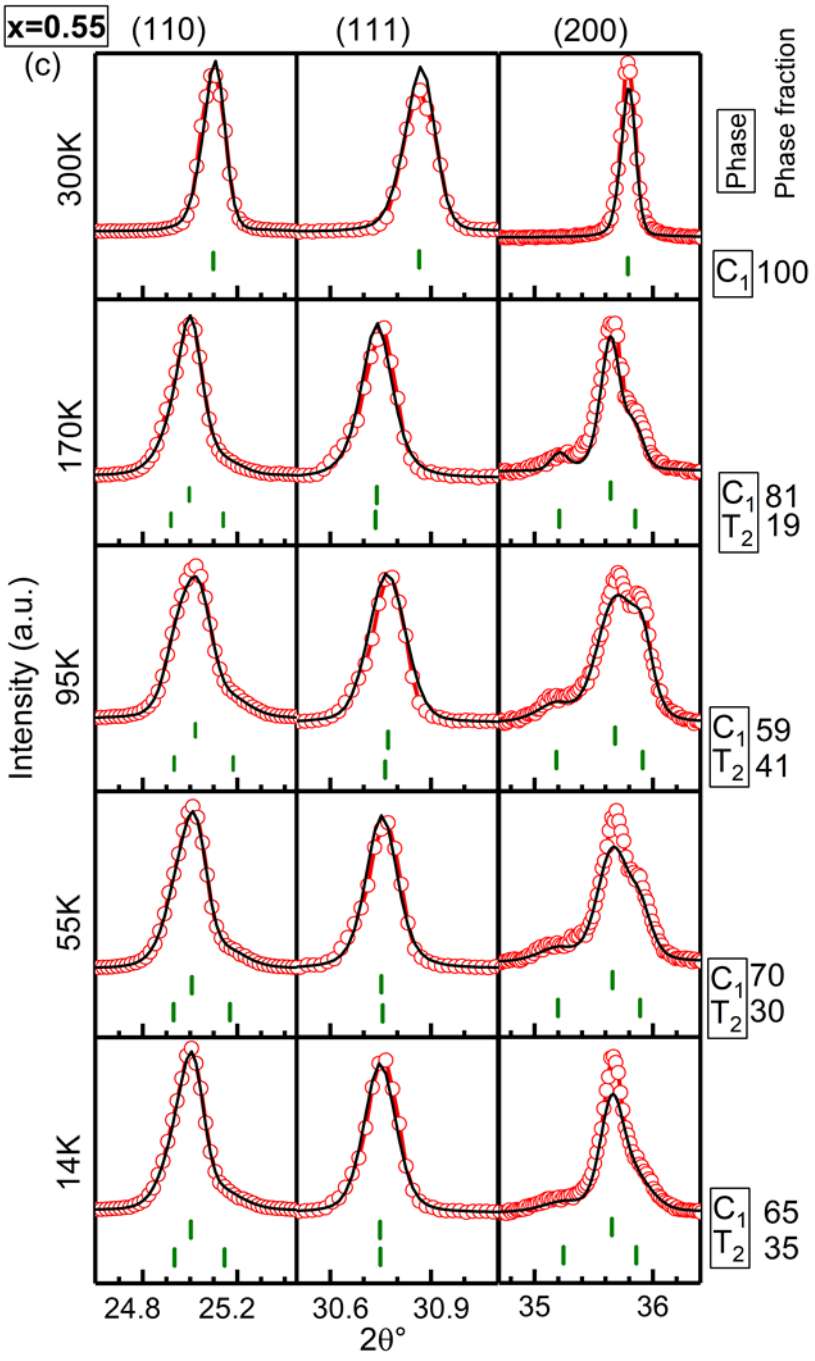

Fig 4.6 (c) Rietveld fit for the pseudocubic (111), (200) and (220) XRD peaks for visualization of crystal structure changes with temperature for x = 0.55 composition

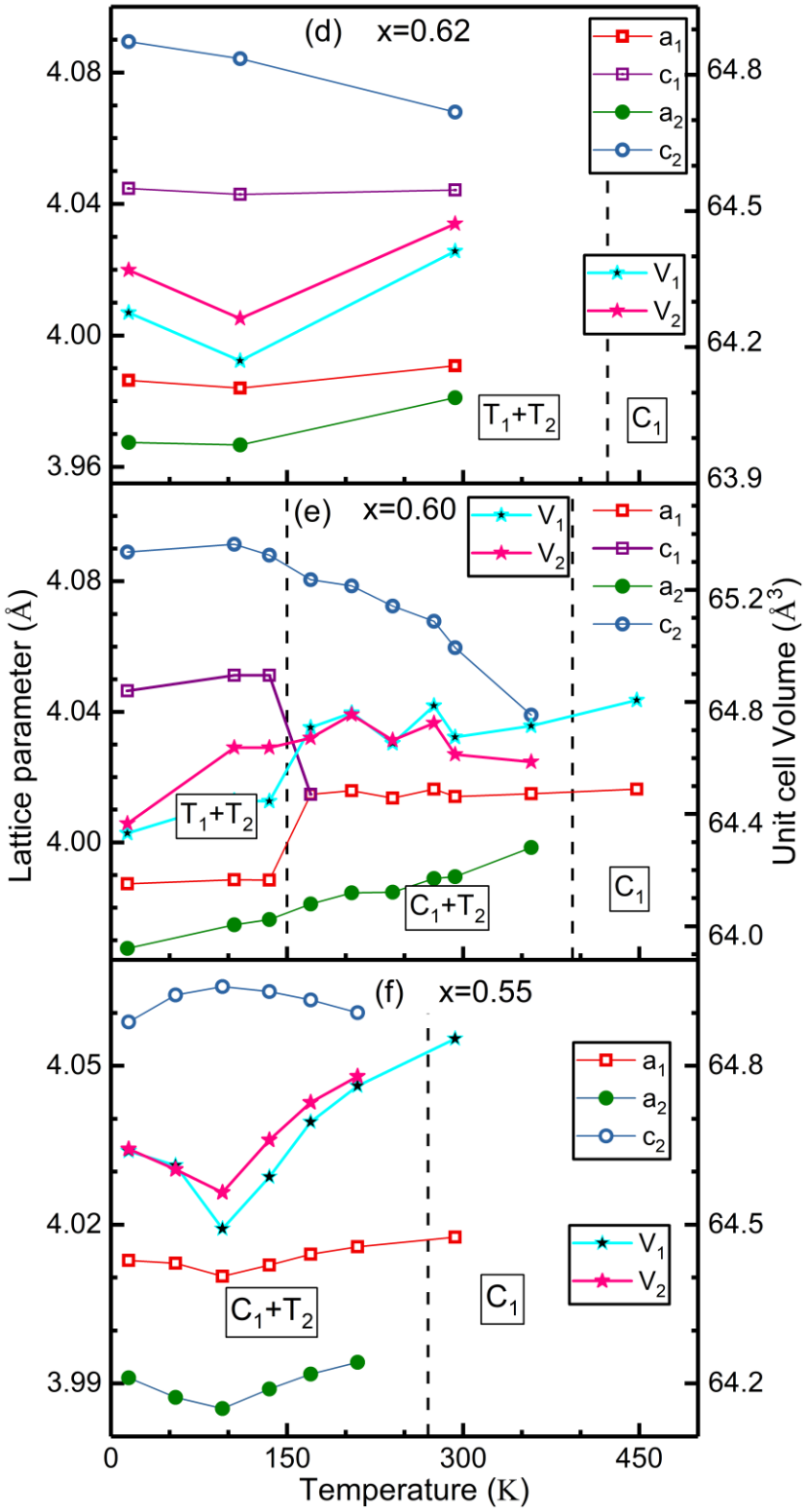

Fig 4.6 Temperature-dependent variation of lattice parameters and unit cell volumes for (d) 0.62, (e) 0.60 and (f) 0.55 composition

Table 4.5 Refined crystal structural parameters of various crystallographic phases in x = 0.62 composition

Temp (K)	a_1 (Å)	c_1 (Å)	V_1 (Å^3)	f_1 (%)	a_2 (Å)	c_2 (Å)	V_2 (Å$_3$)	f_2 (%)
15K	3.9863(4)	4.0447(5)	64.27(1)	20.15(0.89)	3.9674(1)	4.0894(2)	64.34(1)	79.85(1.21)
110K	3.9839(4)	4.0429(8)	64.1(2)	11.35(0.94)	3.9666(2)	4.0842(3)	64.26(1)	88.65(1)
RT	3.9908(2)	4.044(5)	64.41(1)	37.95(1.51)	3.9810(1)	4.0679(2)	64.47(1)	62.05(1.68)

Table 4.6 Refined crystal structural parameters of various crystallographic phases in x = 0.60 composition

Temp (K)	a_1 (Å)	b_1 (Å)	c_1 (Å)	V_1 (Å^3)	f_1 (%)	a_2 (Å)	c_2 (Å)	V_2 (Å$_3$)	f_2 (%)
15K	3.9872(4)	-	4.0464(6)	64.33(1)	22.28(0.94)	3.9675(1)	4.0889(2)	64.366(4)	77.72(0.84)
45K	3.9876(15)	3.9764(15)	4.04238(10)	64.80(5)	51.35(1.66)	3.9692(4)	4.0844(6)	64.34(1)	48.65(0.99)
75K	3.9899(5)	-	4.0546(9)	64.55(2)	48.92(0.26)	3.9733(3)	4.0915(4)	64.59(2)	51.08(0.66)
105K	3.9885(7)	-	4.0511(12)	64.44(3)	60.66(0.98)	3.9747(3)	4.09138(5)	64.63(1)	39.34(1.34)
135K	3.9884(8)	-	4.0511(13)	64.44(3)	65.7(2.56)	3.9763(3)	4.0880(5)	64.63(1)	34.23(1.46)
170K	4.0147(6)	-	-	64.71(1)	22.88(1.22)	3.9810(4)	4.080(6)	64.67(1)	77.12(1.12)
205K	4.0158(4)	-	-	64.76(2)	23.5(0.87)	3.9845(2)	4.0785(5)	64.75(2)	76.4(0.92)
240K	4.0135(7)	-	-	64.65(2)	30.23(1.54)	3.9847(5)	4.0724(8)	64.66(2)	69.77(1.38)
275K	4.0163(3)	-	-	64.78(1)	32.76(1.26)	3.9889(3)	4.0677(6)	64.72(1)	67.24(1.07)
300K	4.0140(1)	-	-	64.67(2)	39.24(0.71)	3.9894(1)	4.0596(4)	64.61(1)	60.76(0.93)
358K	4.0119(9)	-	-	64.57(1)	82.76(1.05)	3.9953(4)	4.0494(11)	64.63(2)	17.24(0.66)
448K	4.0153(1)	-	-	64.80(1)	100	-	-	-	-

Table 4.7 Refined crystal structural parameters of various crystallographic phases in x = 0.55 composition

Temp (K)	a_1 (Å)	V_1 (Å^3)	f_1 (%)	a_2 (Å)	c_2 (Å)	V_2 (Å$_3$)	f_2 (%)
15K	4.0132(1)	64.639(13)	64.82(2.22)	3.9910(3)	4.0582(6)	64.643(13)	35.18(1.61)
55K	4.0127(1)	64.612(4)	69.76(1.59)	3.9873(2)	4.0633(4)	64.604(9)	30.24(0.99)
95K	4.0102(4)	64.492(11)	58.61(0.82)	3.9852(4)	4.0649(7)	64.561(16)	41.39(0.72)
135K	4.0123(2)	64.595(5)	68.59(0.06)	3.9890(6)	4.0654(7)	64.69(29)	31.41(1.23)
170K	4.0144(1)	64.694(3)	81.19(1.34)	3.9917(4)	4.0624(7)	64.731(17)	18.81(0.71)
210K	4.01581(8)	64.762(2)	90.49(1.40)	3.9942(1)	4.0642(7)	64.843(27)	9.51(0.63)
250K	4.0161(5)	64.789(5)	100	3.9890(1)	4.0654(1)	64.69(11)	31.41(0.67)
RT	4.0167(2)	64.80(1)	100	-	-	-	-

4.3.5 Phase Transitions in the Composition Regions $0 \leq x < 0.55$ and $0.90 < x < 1$

The RT crystal structure of BCN is tetragonal, and it persists up to 450°C. After that, a cubic phase starts to emerge and at around 550°C, it changes to a pure cubic structure. An addition of a small amount of PT content in BCN, typically 0.05%, brings down the pseudocubic transition of BCN from 520°C to below RT. Typically, the half of the compositional span of the solid solution ($0.05 \leq x \leq 0.55$) shows cubic symmetry at RT. For this region, the compositions are expected to exhibit a tetragonal structure or coexisting tetragonal and cubic structures below RT, while the composition region $0.62 \leq x < 0.90$ show no significant changes in the crystal structure below RT, except temperature dependent lattice parameter variation of the phases present at RT.

The temperature dependent crystal structure and dielectric study indicate towards the presence of a single thermodynamic system in the composition region $0 \leq x < 0.65$, while it accommodates two phases predominantly in the region $0.80 \leq x \leq 0.90$, whose traces can be found in $0.65 \leq x < 0.80$ and $0.90 < x \leq 0.975$ as well. The $x = 0.95$ and 0.975 compositions show the phase coexistence of two tetragonal structures, both of which are expected to originate from PT-like lattices. The tetragonal to cubic phase transitions in these compositions are expected to appear in the temperature range 480-490°C, as evident from the relative dielectric permittivity responses shown in Fig 4.1.

4.4 Phase Diagram and Phase Transitions in (1-x)BCN-(x)PT Ceramics

Based on the discussion and results presented in preceding sections, a phase diagram has been constructed in Fig 4.7 for the (1-x)BCN-xPT solid solution. To the best of our knowledge, it's the first ever established phase diagram for the ceramics. The two different types of phase coexistence regions are separated by thick grey-

textured vertical lines to demarcate the phase combinations of single-phase cubic (C) and two coexisting cubic phases (C+C). The short-dashed-black lines separate stability regions of different crystal structures observed in different temperature regions while the solid black lines separate the different crystal structures of various composition regions. The vertical nature of these solid black lines separating different crystal structure combination regions also indicate that these phase boundaries are of morphotropic nature. The deep-colored regions around the short-dashed-black lines separated by dotted-grey lines region corresponds to the phase transitions of non-centrosymmetric crystal structures into centrosymmetric ones. The red circles in this deep-colored region show the points where the transition temperature is determined from the dielectric permittivity measurements. Some critical points, where three or more phase boundaries are expected to meet, are also shown in this phase diagram by blue-dotted circles and pink-dotted squares, representing tri-critical and quad-critical points, respectively. A possibility of different type of phase coexistence containing coexisting monoclinic and tetragonal structures, mentioned in Section 4.3.4, is represented by a dashed line extension of the nearby MPB. Out of these seven phase boundaries, two phase boundaries are marked with dashed vertical lines.

Five vertical phase boundaries are visible in Fig 4.7, and two other phase boundaries can be observed on either sides of the cubic phase separating it from tetragonal and the coexisting cubic and tetragonal structures. The compositions in the region $0.62 \leq x \leq 0.90$ of the solid solution possess stable crystal structure below ~450K, i.e., they do not go into phase transformation to any other non-centrosymmetric phases and, therefore, show tendencies to form morphotropic phase boundaries between distinct crystal structures. In addition, the solid solution in this region also offers a very

low thermal expansion, indicating its efficacy as a thermally stable ferroelectric material. These seven different combinations of crystal structures create a lot of opportunities to exploit physical properties near them.

The unusual sort of phase coexistence and phase separation in the solid solution is anticipated to be caused by the existence of polar clusters with significant charge disorder and strain variation as discussed in the next section.

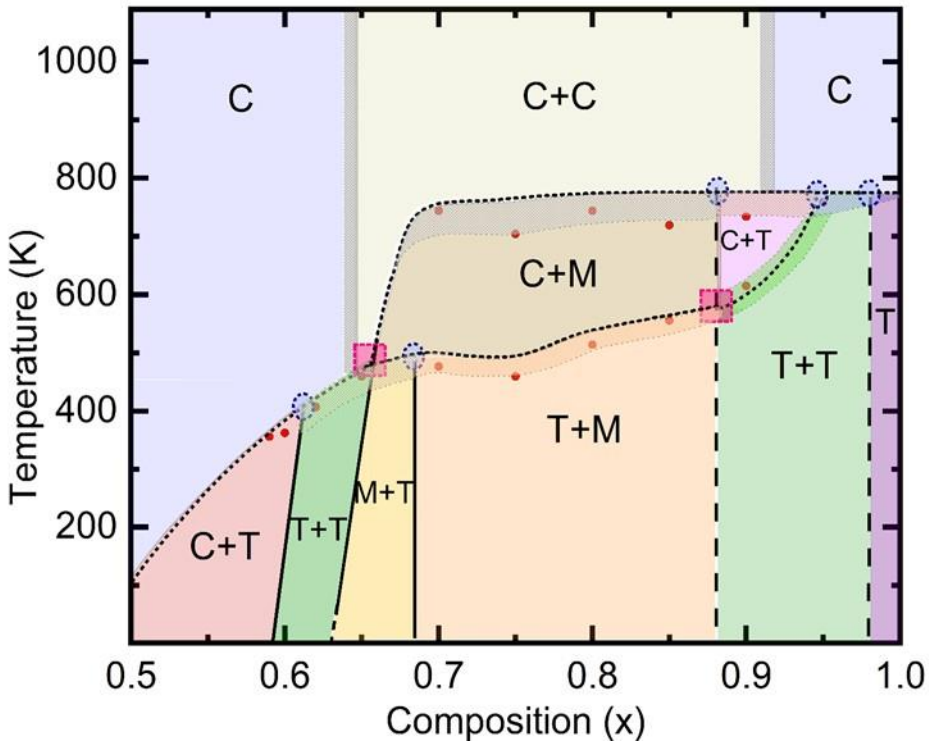

Fig 4.7 Temperature versus composition phase diagram of (1-x)BCN-(x)PT ceramics

4.5 Phase Dynamics in (1-x)BCN-(x)PT Ceramics

4.5.1 Phase Coexistence and Phase Separation in (1-x)BCN-(x)PT Ceramics

As previously observed in Section 3.8, the unit cell volume difference between the two coexisting phases of the solid solution changes as the composition varies, while

on the other hand, for the $0.70 \leq x \leq 0.90$ composition region, it remains almost unaffected by temperature variations (15K to ~773K). As evident from the XRD measurements, a two-phase coexistence has been observed in the solid solution, with varying extents of phase separation between the phases in terms of unit cell volume differences. The high degree of unit cell volume difference in this region is the primary cause of the phase separation.

Over the years, numerous models have been discussed in the literature to help understand the phenomenon of phase coexistence in ferroelectric perovskite solid solutions and how it relates to the physical features of these materials. These models revolve around the concepts of MPB [78], Polymorphic Phase Boundary (PPB), adaptive phases by miniaturization of domains [10,25,96], coherent phase interfaces [87], phase separation [97,98], sub-micron level structural heterogeneities [17,99], positional lattice site heterogeneities [17,85], composite phase formation, random phase fields [99], spatial compositional variance (concerning both statistical and solubility gaps) [17,20,85], local distortion around Pb-ion in Pb-based solid solutions [85], etc. Furthermore, some of the terms coined in the phase coexistence domain concerning the different ionic sizes of the 'B' site cations in perovskite structure are local strain variations, different polar clusters, incomplete diffusion, etc. [10,17] Each of these notions was supported by theoretical modelling [20,100] as well as structure probing experiments, such as X-ray diffraction [25,85,87,101], neutron diffraction, raman scattering [85,102], SEM [103], EDX, SAED and domain visualization via TEM [25,87,100,101,103], etc. This thesis mainly inspects the phase coexistence/separation phenomena by means of the temperature-dependent XRD experiments while speculating it using EDS, XPS and dielectric measurements. Moreover, the following

are examples of coexisting phases in different contexts. One can observe that in metallic glasses, for example, $La_{27.5}Zr_{27.5}Al_{25}Cu_{10}Ni_{10}$, two coexisting solids can be found converting into two other different solids having a slight compositional variation [104]. Such phase coexistence is often addressed as phase separation in these alloys. In $K_{0.8}Fe_{1.6}Se_2$ single crystals, a frustrated type phase separation is evident in the Synchrotron single-crystal TEM mode SAED between a tetragonal lattice with Fe-ion modulated magnetic phase and another lattice containing a superstructure of a non-magnetic phase at 520K. The two crystal structures appear for a short temperature range, and both crystallographic phases show different physical properties [105,106]. Another example, although only theoretically predicted, is the phase diagram of $Li(Al_xCo_{1-x})O_2$ composition, where a unique kind of phase separation sequence is expected from ab-initio pseudopotential methods in which two different solids co-exist at RT. They can be converted into one single-phase solid material at a high temperature and further into two other solids with increasing temperature due to enthalpy variations [107]. In some metal oxides, especially rare-earth cuprates and manganites, the phase separation (compositional and electronic type) is frequently evident phenomenon. [73,97,98,108,109] Furthermore, the phase separation is also observed in ferroelectric oxides (in the form of the hetrostructural fluctuations in first-order transitions) [110–112] and in some phospholipids [113]. In all the cases where phase separation is found between the coexisting phases, the difference in the order parameter (with respect to which the separation between the phases is realized, such as electronic properties, compositional variance, etc.) is usually small.

The solid solution (1-x)BCN-(x)PT is one of its kind as it finds similarities and differences from the usual Pb-based ferroelectric perovskite ceramics studied till date.

This can be understood by the temperature dependent phase evolution instances of the x = 0.60 and 0.85 composition of (1-x)BCN-(x)PT. In the 0.60 composition, a single cubic crystal structure is observed at high temperatures as a result of a ferroelectric to paraelectric phase transition, while the composition also shows two coexisting tetragonal phases at cryogenic temperatures. Interestingly, in the 0.85 composition, two centrosymmetric cubic phases (indicated as C+C in Fig 4.7) containing large volumetric differences (~1.3$Å^3$) have been observed at very high temperatures (~1073K). This type of temperature dependent phase transition is rare to find in the Pb-based ferroelectric perovskites.

In perovskite-structured solid solutions, it is typically the case that, at substantially elevated temperatures, single-phase cubic or other higher symmetry crystal structures are obtained. It is a consequence of the natural thermal expansion of the lattice, providing sufficient space for the constituent ions to organize themselves in an ideal cubic perovskite structure with a Goldschmidt tolerance factor equal to 1 [13]. This can lead to phase coexistence around some particular temperature range due to the first-order thermodynamic phase transition between a high-temperature phase with higher crystallographic symmetry and a lower-temperature phase with lower symmetry. This may or may not be associated with the MPB, PPB or any other sort of phase coexistence.

It is important to note that compositions prepared under the same synthesis conditions with the same type of chemical reactants do not result in such phase coexistence at high temperatures, but give a single-phase cubic structure, e.g., x = 0.20 to 0.65. The compositional integrity of the solid solution has been examined in the sintered samples by EDX for a selected composition, i.e., x = 0.80, which had the

maximum phase separation. Any possibility of the formation of a macroscale composite phase structure is ruled out, as evidenced by the EDS compositional analysis (Section 5.3) of the samples, which confirms the macro-scalar homogeneous distribution of elements. The XPS analysis (Section 5.3) confirm the nominal oxidation states of all the elements of the solid solution.

In the well-known relaxor ferroelectric $Pb(Mg_{1/3}Nb_{2/3})O_3$, it is reported that the ratio of B-site cations matches the nominal composition for a disordered region of the sample as well as for a nano-polar chemically ordered region, as confirmed from a nano-sized EDX [114]. However, the phase coexistence in the 0.85 composition indicates the formation of two closely entangled thermodynamic systems due to large strain variations in such compositions, finding the similarity to usual way of strain accommodation leading to phase coexistence in hetrostructural ferroelectrics [112].

4.5.2 Polar Cluster Formation and Random-Site Model

The polar character in BCN mostly arises because of the relative displacement of the B-site cations and the B-O_6 octahedra since the distortion around Ba-ion does not substantially contribute in polarization due to its closed shell structure. The deviation from average symmetry caused by the random distribution of polar clusters can have an impact on the diffraction intensity in terms of a reduction of the main peak and increased diffuse scattering, resulting in broad XRD peaks [17]. Similarly, the pure BCN compound calcined at 900°C has much broader peaks with insufficient resolution of the peaks splitting, while sharp intensity peaks have only been observed after high temperature (≥1150°C) sintering [55]. In BCN and its solid solutions, the formation of polar clusters is commonly reported as a result of the substitution of both A-site and B-site ions [55,115]. The formation of ordered structures in the (1-x)BCN-(x)PT system is

also ruled out on the basis of the absence of any XRD satellite peaks (Fig 1.14(c) and (d)). The absence of ordering in the BCN also implies that niobium and copper ions are distributed randomly at the octahedral positions. The ionic radii for Nb and Cu-ion in the octahedral sites are 0.64Å and 0.73Å, respectively. This difference may get further modified in the presence of Ti-ions during solid solution formation with PT and may create strain variation between the unit cells similar to what is observed in PZT and explained in terms of the distribution of lattice parameters and the resulting anisotropic peak broadening of the diffraction profiles [17]. The crystal structure and physical properties have often been correlated with the existence of many different types of clusters in PZT-like disordered crystal-structured ceramics. To understand the mechanics of PZT and like systems, researchers have used terminologies like polar clusters, nanoclusters, nanodomains, nanopolar areas, spatial compositional variation, sub-micron level chemical inhomogeneities, etc., to address the consequences of ionic size variation of atoms in the literature [17,116,117]. The presence of the different-sized nanocluster produces a strain field, which also leads to diffuse scattering and low resolution in the splitting of pseudocubic peaks [17,111]. Some of such evidences in (1-x)Ba(B',Nb)O_3-y$PbTiO_3$ [B' = Zn (0.74Å) , Mg (0.72Å), Sc (0.75Å)] based solid solutions can be seen near $0.80 < y < 0.90$ comprising unusual broadening in XRD peaks [64,65,118].

Despite the fact that there are global homogeneities in elemental image inspection of the (0.20)BCN-(0.80)PT, this random distribution may nonetheless result in some spatial variation in the distribution of ions to still occur at nanoscale, which leads to the formation of nanoscale clusters. The phase separation in the solid solution can be correlated to the tendency to form polar clusters in the BCN-type lattice along

with the PT-type lattice. Multi-ion substituted B-site cations forming complex perovskite solid solutions exhibit disordered distributions, referred to as compositional, chemical or substitution disorders, especially in $A(B^{+2\prime}B^{+5\prime\prime})O_3$ type systems [119]. The temperature and time of processing are also crucial factors in such systems. Disordering due to thermal quenching and an unrealistic time for the homogenized ordering is basically result in the absence of the ordering in such complex solid solutions [119,120].

For these type of materials, a "random-site" model has been proposed by Bokov et al in 2006, where the overall charge and stoichiometry are balanced by the clustering of one particular (B-site) ion on a very short scale while surrounding it with a random distribution of both the B-site ions leading to a local B´ rich nanoclusters [119]. Since there were no other impurities or any solubility gap present in the solid solution, it can be inferred that distinct clusters of Cu and Nb-ions, with B-site cations, continue to form randomly, even after the addition of Ti ions in higher concentrations. In a similar case, as reported by Levin et al., Ti in low concentration in the $Ba(Zr_{(1-x)}Ti_x)O_3$ solid solution tends to occupy bigger centrosymmetric lattices without clustering, whereas in high concentration, it forms nano polar clusters (non-centrosymmetric unit cells) and for the intermediate compositions, it may exhibit both characteristics [117]. Conclusively, the solid solution may possess different types of nano-polar regions and ion clusters, and local probe based further studies are essentially needed to confirm and completely understand the different phenomena taking place in the (1-x)BCN-(x)PT system.

4.5.3 Diffraction Artefact and Nano-Domain Approach

In the case of the (1-x)BCN-(x)PT solid solution, the chemistry has been observed to be potentially affected by the phase stability, and the formation of clusters is also predictable given the significant ionic radii differences among the B-site copper,

titanium and niobium ions. The typical phase separation in the solid solution is an indication of the presence of two unit cells with different unit cell parameters from the XRD pattern analysis and therefore, different stain fields can be predicted to exist within them, unless the diffraction pattern itself does not truly represent the local symmetry of the system due to diffraction artefact. The diffraction artefact is actually the alteration in the interference phenomenon of the diffracted x-rays from nanodomains of reduced coherence length, which causes certain diffraction pattern peaks to appear/disappear, leading to an incorrect interpretation of local crystal structural symmetry [10,25,85,96,101,121,122]. A material having nanoscalar domains, the XRD is unable to accurately represent the genuine local structure and instead provides an average structure because of this short coherence length. This phenomenon is widely reports in PZT and PMN-xPT-like ceramics, where the rhombohedral-tetragonal phase coexistence near the MPB may be predicted as a monoclinic one. Although the extended Devonshire theory can successfully accommodate existence of monoclinic phases in these systems by considering the free energy expansion up to the 8^{th} order. Some authors believe that the appearance of monoclinic phases is just the conformal miniaturization of the nano-domains and thus just an diffraction artefact [11,25]. This monoclinic phase of adaptive form is driven by the elastic compatibility accommodation of specific geometric arrangements of nanodomain clusters. They can be categorized into three types depending on the accommodation of stress. In the partial and complete stress accommodation states, some special invariant conditions of the lattice parameters need to be followed [122].

As speculated in the previous subsection, that the solid solution (1-x)BCN-(x)PT ceramics may consist of NPRs, the presence of coexisting monoclinic may be expected

to possess the same origin as in adaptive form. To check any possible correlation of the monoclinic phases found in the composition region $0.75 \leq x \leq 0.85$ of the (1-x)BCN-(x)PT solid solution, the lattice parameter variations have been carefully examined, considering both types of invariance condition fulfilment as well as the fitting of a cubic phase instead of a monoclinic one. Additionally, the relaxations in the invariance conditions for some compositions arising due to the high density in stacking faults or impurity phase fraction may be assumed to be taking place, but the lattice parameters of the monoclinic phase do not fall anywhere near the actual invariance conditions for the consideration of relaxation phenomenon. Therefore, it can possibly be inferred that the monoclinic phase of the (1-x)BCN-(x)PT solid solution does not have any similarities with the monoclinic adaptive phase. Moreover, the absence of macro-scalar inhomogeneities in the elemental mapping of individual atoms in monoclinic-tetragonal phases (for 0.80 composition) having large phase separation also rules out any resemblance to the case of martensite-type phase appearance in metals and alloys.

In conclusion, the phase coexistence in MPB ceramics and appearance of monoclinic phases are still a matter of great debate. A major part of the research community believes that the monoclinic phases in MPB ceramics arise due to thermodynamic phase transitions and leads to the phase coexistence with the parent phase because of the first order nature of the phase transition. Many authors, however, believe that the strain accommodation of the adaptive phases near MPB and conformal miniaturization of the nano domains leads to the diffraction artifact manifesting itself as the monoclinic phases in the diffraction measurements. The (1-x)BCN-(x)PT system can be a model system to settle this issue, as our investigations reveal that both of these

kind of phases coexistence and monoclinic phases appearance may exist in it for different composition range.

4.6 Conclusion

A new solid solution has been investigated for its temperature-dependent crystal structures. A phase diagram of the solid solution has been established at a common sintering temperature of 1050°C. The solid solution has been shown to consist of a novel type of crystal structure where two-phase coexistence has been observed in a wide composition range, $0.59 \leq x \leq 0.975$, with two different kinds of phase coexistence. The phase separation in the tetragonal and monoclinic phases is also larger than ever reported in any PT-based ceramic solid solution. The first is the most common type found in the perovskites, which originates from the first-order thermodynamic phase transition, predominantly found in the compositional region $0 \leq x \leq 0.70$, $0.90 < x \leq 1$, whereas the second observed in $0.75 \leq x \leq 0.90$ possess phase separation and finds its similarities more with quenched and compositionally disordered type complex perovskite solid solutions. The phase separation in the solid solution was found to vary with composition and synthesis conditions, whereas it remains almost constant for a composition within a reasonable temperature range (15K to 1073K). The presence of seven phase boundaries in the solid solution shows its importance as a ferroelectric ceramic. The observed monoclinic phases in the phase-separated region of the solid solution do not fall into the criteria of adaptive phase formation; instead, the origin of the two-phase coexistence and phase separation between them is correlated with cluster formation at the sub-micron level to accommodate stress. The negligible thermal expansion characteristics of the solid solution have the potential to be used in industries demanding low fatigue over wide temperature ranges, typically 15K to 773K.